High-Performance SOI-Based Filter with Multiple Microring Resonators for Telecom Applications: Design, Fabrication, and Characterization

Hamed Saghaei, Member, IEEE, and Kambiz Moez, Senior Member, IEEE

Abstract—In this paper, we present the design, simulation, fabrication, and characterization of a high-performance all-optical filter. It consists of three cascaded microring resonators and four integrated grating couplers, developed for precise wavelength selection within the telecom band (1500-1600 nm). The device was fabricated on a silicon-on-insulator platform using highresolution electron beam lithography and encapsulated with a silica cladding layer to enhance mechanical robustness and increase the effective refractive index, resulting in superior optical performance. A fundamental aspect of the proposed design is systematic geometrical tailoring of critical parameters, including ring radius, waveguide width, coupling gap, coupling length, and the number of cascaded resonators, to allow precise control over the filter's spectral characteristics. The fabricated filter achieves an ultra-narrow passband of 1.99 nm, a resonance power transfer efficiency exceeding 56%, and a Q-factor up to 804. The free spectral range (FSR) is shown to be designdependent, varying between 27 nm and 37 nm as a function of ring radius, thus enabling flexible specification during the design phase. Experimental characterization using tunable lasers showed strong agreement with finite-difference time-domain simulations, validating the filter design. Extensive parametric studies were conducted to evaluate the influence of structural variations on key performance metrics, including resonance wavelength, Q-factor, transmission efficiency, and FSR. The proposed filter demonstrates outstanding spectral resolution, low insertion loss, and excellent efficiency, establishing it as a promising solution for advanced optical communications, high-precision photonic signal processing, and emerging nanophotonic systems.

Index Terms—All-optical filter, Ring resonator, Grating coupler, Silicon-on-insulator, Electron beam lithography, Free spectral range, Quality factor, Finite-difference time-domain.

I. INTRODUCTION

ODERN optical communication systems face increasing challenges such as limited scalability, high power consumption, large device footprints, and the growing demand for higher data transmission speeds [1]–[4]. Photonic Integrated Circuits (PICs) have emerged as a transformative solution to these challenges by integrating multiple optical and electronic functionalities onto a single compact chip [5]–[8]. PICs offer improved scalability, reduced energy consumption, and enhanced performance, making them an essential component of next-generation high-capacity and energy-efficient communication networks [9]–[12]. PICs are typically made from silicon or III–V semiconductor materials because of their excellent optical and electronic properties [10], [13].

H. Saghaei and K. Moez are with the Department of Electrical and Computer Engineering, University of Alberta, Edmonton, AB T6G2R3, Canada Manuscript received April XX, 2025; revised XX, 2025.

They integrate various components, including lasers, photodetectors, modulators, amplifiers, splitters, and especially optical resonators [6], [8]. Among these components, optical ring resonators play a critical role due to their versatility in applications such as wavelength filtering [14]-[19], optical modulation [20], [21], signal processing [22], delay lines [23]– [25], and sensing [26]–[31]. Ring resonators consist of a circular waveguide connected to one or more linear bus waveguides. They work based on optical resonance, meaning that only certain wavelengths of light, which match the resonance conditions, enter and circulate within the ring. These resonant wavelengths are then guided to the Drop port while other wavelengths pass through the bus waveguide and exit via a through port. This selective wavelength routing capability highlights the importance of ring resonators and makes them a vital part of advanced photonic systems.

One of the pioneering optical ring resonator structures was demonstrated by Haavisto and Pajer (1980) [32]. In their study, polymeric waveguides made of PMMA with a width of 10 µm and a center-to-center spacing of 17.5 µm were utilized, and the resonator had a radius of 4.5 cm. Prism coupling was employed to couple light into the waveguides, achieving a coupling coefficient of 2% and an overall propagation loss of 0.05 dB cm⁻¹. Nevertheless, due to its large dimensions, the applicability of this resonator as a channeldropping filter was limited. This work is recognized as a foundational contribution, paving the way for subsequent developments in ring-resonator-based optical filters. Advances in fabrication technologies and the development of novel III-V semiconductor material systems have enabled the realization of compact ring resonators with dimensions below 100 µm. A notable early demonstration by Rafizadeh et al. (1997) [33] presented AlGaAs/GaAs-based ring and disk resonators with diameters of $10.5 \,\mu\mathrm{m}$ and $20.5 \,\mu\mathrm{m}$, respectively. For a $10.5 \,\mu\mathrm{m}$ disk resonator, a free spectral range (FSR) of 21.6 nm and a full width at half maximum (FWHM) of 0.18 nm were measured, yielding a finesse of 120 and a Q-factor exceeding 8500. A ring resonator of the same size showed an FSR of 20.6 nm and FWHM of 0.43 nm, corresponding to a finesse of 48 and a Q-factor above 3500. Grover et al. (2002) [34] demonstrated an optical channel drop filter based on threering resonators fabricated on GaAs-AlGaAs and GaInAsP-InP platforms. These structures exhibited FSRs of 30 nm and 40 nm, respectively, achieving three to four times the FSR of a single-ring resonator. Bogaerts et al. (2012) [35] presented a comprehensive review of silicon microring resonators,

providing an in-depth theoretical background and highlighting their compact structure and broad applicability in photonics. Despite their advantages, these resonators face performance limitations due to environmental sensitivity, fabrication complexity, and optical losses. Krasnokutska et al. (2019) [36] focused on the design and fabrication of tunable microring resonators on Z-cut lithium niobate on insulator platforms. They developed low-loss, single-mode waveguides and fabricated microrings with radii ranging from 30 µm to 90 µm. These resonators demonstrated FSRs up to 5.7 nm and broad resonance bandwidths. Challenges included high sensitivity to fabrication accuracy, significant TE-mode bending losses, narrow coupling gaps, complex modeling requirements, and high operational voltages. Tran et al. (2020) [37] developed tunable semiconductor lasers with ultra-narrow linewidths based on ring resonators on a heterogeneous Si/InP platform. Their second-generation design achieved a 220 Hz linewidth and 110 nm tuning range across the S, C, and L bands. While offering advantages like broad tunability and low phase noise, challenges included thermal crosstalk, limited output power, and scalability. Selim and Anwar (2023) [38] demonstrated an optical filter based on nested silicon microring resonators composed of an open ring and a racetrack resonator. This design achieved a four-fold improvement in the Qfactor and is suitable for sensing and delay-line applications. However, it still faces challenges in fabrication complexity and environmental stability. Saha et al. (2024) [39] reviewed silicon photonic filters, emphasizing CMOS compatibility, low power consumption, and tunability. However, precise nanometer-scale fabrication remains a challenge, significantly affecting reproducibility and performance. Photonic crystal ring resonators (PCRRs) are studied for high-Q filtering, sensing, and communication applications [40]–[42]. However, they are highly sensitive to fabrication imperfections, material losses, and radiation losses from bends. Coupling efficiency is difficult to optimize, and PCRRs require advanced simulation techniques such as finite-difference time-domain (FDTD) and Plane wave expansion (PWE), which are computationally expensive. Integration with other photonic components and temperature sensitivity further complicate their practical deployment. Despite progress, optical ring resonators still face major challenges: sensitivity to fabrication errors, optical losses from absorption and roughness, limited resonance bandwidth, interring crosstalk, and complex modeling requirements. Thermal and environmental sensitivity remain critical barriers. Recent advances in silicon photonic filters have explored a variety of coupled-resonator optical waveguide (CROW) architectures to achieve high-performance and tunable spectral characteristics. For instance, reconfigurable microwave photonic bandpass filters based on CROW structures have demonstrated dynamic control over filter responses, making them attractive for RF-photonic integration [43]. Similarly, wideband multistage CROW filters have been proposed with a focus on relaxed fabrication tolerances, enabling scalable and robust implementations suitable for mass production [44]. Kumar and Tsang (2021) [45] developed a high-extinction on-chip optical filter using cascaded CROW structures on silicon-on-insulator (SOI), achieving over 96 dB suppression of pump photons

for quantum photonics. The filter offers tunable bandwidth via thermal phase shifters, combining compactness, low loss, and integration suitability. In another development, a compact high-contrast optical filter has been realized using all-passive CROW configurations combined with Fano nanobeam resonators, offering sharp spectral features and low insertion loss without the need for active tuning elements [46]. These efforts highlight the growing interest in passive, high-performance CROW-based filter designs, motivating further exploration into alternative cascaded resonator configurations with enhanced spectral control and fabrication resilience.

In this paper, we propose a compact and high-performance optical filter based on three cascaded microring resonators integrated on the SOI platform. The principal novelty of this work lies in the use of cascaded decoupled microrings, resulting in a significant enhancement in drop-port performance compared to conventional single-ring filters. In the proposed structure, optical power that is not coupled into the first microring continues to propagate through the bus waveguide and is subsequently coupled into the second and third microrings. Each ring extracts additional power and transfers it to the drop port, leading to a cumulative increase in output power. This mechanism contributes to improved transmission efficiency and a higher Q-factor, while maintaining design simplicity. The microrings are arranged side by side with sufficiently large center-to-center spacing to ensure that inter-ring coupling effects are completely suppressed. Unlike earlier multi-ring designs that rely on tight coupling or intricate geometries, the proposed filter maintains a simple, circular microring layout and adopts passive design principles that are fully compatible with standard silicon photonic fabrication processes. To support the claimed performance improvements, we derived scalable analytical expressions calculating the drop/through transmissions of multi-ring filters and extensively simulated the proposed structure using numerical FDTD solvers. The proposed filter presents a practical and reliable solution for achieving high-Q, low-loss optical filtering in silicon photonic integrated circuits, enabled by its CMOS-compatible fabrication process and complete experimental validation.

II. PROPOSED FILTER

A. Filter Structure

The proposed silicon photonic filter, depicted in Fig. 1(a), employs a cascaded arrangement of three microring resonators integrated with two bus waveguides and four grating couplers. This cascaded configuration enhances wavelength selectivity and spectral efficiency compared to conventional single-ring designs, reflecting a novel approach presented in this study. The entire structure is fabricated from silicon and positioned on a silica (SiO₂) substrate. A protective silica cladding is applied over the device, significantly improving mechanical durability, environmental stability, and optical performance, as well as optimizing the effective refractive index.

The filter operates by selectively routing specific wavelengths through resonant interactions within the cascaded microring resonators. Light entering via an input grating coupler propagates along the waveguide, interacting sequentially with

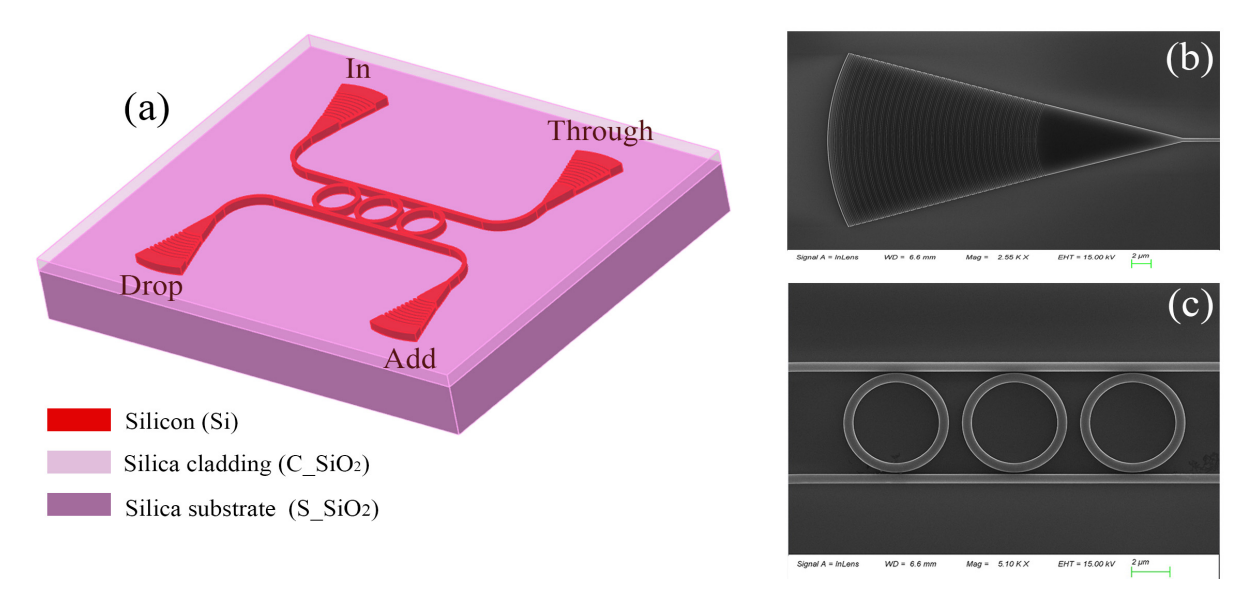


Fig. 1. (a) Schematic of the proposed silicon photonic filter consisting of cascaded microring resonators and grating couplers. (b) SEM image of the fabricated grating coupler. (c) SEM image of the cascaded microring resonators.

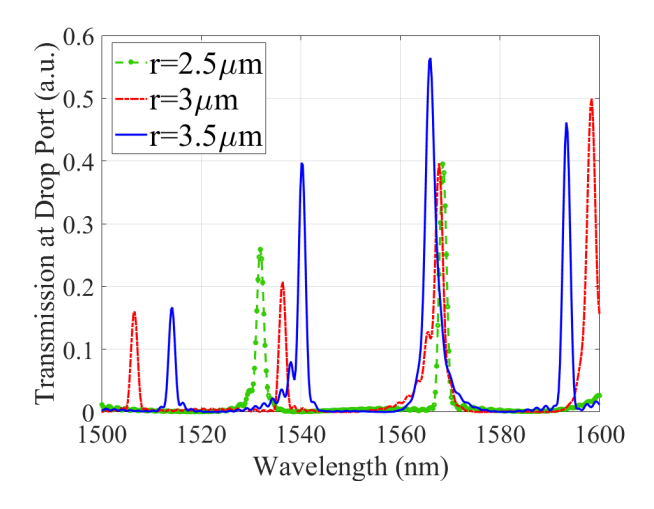


Fig. 2. Transmission spectra at the *Drop* port for the silicon photonic filter with cascaded microring resonators with radii of $2.5 \mu m$, $3 \mu m$, and $3.5 \mu m$.

each microring resonator. Resonant wavelengths couple into the rings and are guided to the *Drop* port, exiting via an output grating coupler. Non-resonant wavelengths bypass the resonators and leave the structure through the *Through* port, connected to another grating coupler. This design ensures precise wavelength selection and efficient operation, making it highly applicable in optical modulation, photonic signal processing, and optical communication systems.

Scanning electron microscopy (SEM) imaging was performed to verify the precision and quality of fabrication. Figures 1(b) and 1(c) display SEM images of the grating couplers and microring resonators, highlighting excellent dimensional accuracy, precise component alignment, and high-quality fabrication. The careful control during lithography and silicon etching processes ensures robust and reliable device performance.

B. Fabrication Process

The proposed silicon photonic filter based on microring resonators was fabricated on a silica (SiO₂) substrate using EBL technique, enabling precise nanoscale structuring essential for PICs. Initially, a silica substrate approximately 2 µm thick was prepared to minimize optical losses and optimize waveguide performance. The wafer surface was cleaned thoroughly using acetone and isopropanol, followed by oxygen plasma cleaning (O₂ plasma) to eliminate any residual surface contamination. Subsequently, a thin silicon layer (220 nm) was deposited onto the silica substrate via plasma-enhanced chemical vapor deposition (PECVD). A positive photoresist (PMMA) was then applied using spin coating at 3000-5000 rpm, creating a uniform resist layer 100 nm to 300 nm thick. The wafer was subjected to a soft bake at 90 °C to 110 °C to remove solvents and moisture, preparing it for the lithographic step. EBL was employed to define patterns for waveguides, microring resonators, and grating couplers on the PMMA layer. An electron beam generated by an electron gun was precisely focused onto selected areas, breaking polymer chains within the resist and altering its chemical properties. Following exposure, the pattern was developed by immersing the wafer in an MIBK:IPA solution (1:3 ratio). In this step, exposed regions of the PMMA were dissolved, clearly revealing the designed patterns on the substrate. The defined patterns were transferred to the silicon layer using reactive ion etching (RIE). The sample was etched in a plasma chamber containing SF₆ and C₄F₈ gases. SF₆ served as the primary etching agent, removing selected silicon regions, while C₄F₈ provided protection against excessive etching, ensuring vertical sidewalls and accurate pattern transfer. After etching, residual photoresist was fully removed through O₂ plasma ashing, resulting in a clean and precise final structure. Scanning electron microscopy (SEM) imaging was performed to evaluate fabrication quality, dimensional accuracy, and alignment, with representative images shown in Figs 1(b) and 1(c). Finally, a protective silica

cladding was deposited using PECVD, covering the entire photonic structure. This protective layer enhanced mechanical and environmental stability and optimized optical performance by increasing the effective refractive index. The final structure exhibited minimal surface and sidewall roughness along with excellent dimensional conformity to the original design specifications. These characteristics led to reduced scattering-induced losses and enabled the fabricated device to closely replicate the simulated model under realistic conditions [47], [48]. The strong agreement between experimental results and numerical simulations confirms that the highly accurate design effectively predicted and reproduced the optical behavior of the proposed structure.

C. Key Parameters

Key filter parameters, including resonance wavelengths, free spectral range (FSR), spectral bandwidth, quality factor (Qfactor), and insertion losses, were extracted from the measured spectra. Resonance wavelengths were clearly identifiable by pronounced transmission peaks at the *Drop* port and corresponding transmission minima at the *Through* port. The FSR, representing the wavelength separation between consecutive resonances, was determined by calculating the wavelength differences between adjacent resonance peaks. These parameters collectively characterize the photonic filter's performance and are essential for assessing its suitability in advanced photonic systems. In symmetric photonic circuits, the FSR typically remains consistent and directly depends on the geometric parameters and material composition of the resonator. The FSR critically influences filter performance, and its desirability varies based on the intended application. A larger FSR results in wider spacing between consecutive resonant wavelengths, leading to a lower mode density. This characteristic is particularly beneficial in wavelengthselective filters and DWDM systems, as it enhances wavelength separation and minimizes crosstalk, thereby improving signal integrity and overall system performance. Conversely, a smaller FSR results in closely spaced resonant wavelengths, which is advantageous for optical sensing, precision filtering, and mode-locked lasers, where sensitivity to subtle wavelength shifts is essential. However, an excessively small FSR may lead to mode interference, reduced filter selectivity, and other detrimental photonic effects. Therefore, determining the optimal FSR involves careful consideration of the specific application requirements, resonator design, and the targeted photonic system. The FSR is calculated using the following relation:

$$FSR = \frac{\lambda_{res}^2}{n_a L} \tag{1}$$

where $\lambda_{\rm res}$ denotes the resonance wavelength, and L is the circumference of the ring resonator [49]. The FSR is intrinsically linked to the resonator's dimensions and critically defines the operating wavelength range of the photonic filter. $n_g(\lambda_0)$ is the group refractive index at λ_0 , which is used instead of the effective refractive index $n_{\rm eff}$ because it accounts for the

dispersion characteristics of the waveguide. It is calculated as follows:

$$n_g(\lambda_0) = n_{\text{eff}}(\lambda_0) - \lambda_0 \frac{dn_{\text{eff}}}{d\lambda}$$
 (2)

The quality factor (Q-factor) is another fundamental parameter for evaluating the performance of silicon-based ring resonators. It characterizes the sharpness and intensity of optical resonances, representing the ratio of stored energy within the resonator to the energy dissipated per oscillation cycle. Consequently, the Q-factor significantly influences energy losses, wavelength discrimination accuracy, and overall efficiency in photonic systems. In an add-drop ring resonator, the ring cavity is coupled to two bus waveguides via directional couplers characterized by amplitude self-coupling coefficients r_1 and r_2 , and cross-coupling coefficients κ_1 and κ_2 , respectively. These coupling coefficients satisfy the energy conservation condition:

$$\begin{cases} \kappa_1^2 + r_1^2 = 1\\ \kappa_2^2 + r_2^2 = 1 \end{cases}$$
 (3)

The Q-factor is mathematically expressed as:

$$Q = \frac{\lambda_{\text{res}}}{\Delta \lambda} \tag{4}$$

where $\Delta\lambda$ is the FWHM of the resonance peak in an add-drop ring resonator and is a key parameter that determines the filter's resolution [35]. It can be expressed as:

$$\Delta \lambda = \frac{(1 - r_1 r_2 a) \lambda_{\text{res}}^2}{\pi n_q L \sqrt{r_1 r_2 a}} \tag{5}$$

This relationship quantitatively defines the resonator's performance and guides the optimization of photonic device design. In ring resonator-based filters, a high Q-factor indicates superior performance in wavelength selectivity, reduced optical losses, and enhanced overall system efficiency. High-Q filters can transmit specific wavelengths with high precision while effectively suppressing others. This characteristic makes them highly suitable for applications such as optical communications, photonic sensing, and PICs. Conversely, a low Q-factor implies rapid leakage of optical energy from the resonator, limiting its ability to confine light for a sufficient duration. This, in turn, degrades the filter's performance in terms of wavelength discrimination and efficiency. The finesse \mathcal{F} is defined as the ratio of the FSR to the FWHM $\Delta\lambda$. It characterizes the sharpness or quality of resonances relative to their spacing and is expressed mathematically as:

$$\mathcal{F} = \frac{\text{FSR}}{\Delta \lambda} = \frac{\pi \sqrt{r_1 r_2 a}}{1 - r_1 r_2 a} \tag{6}$$

Structural losses significantly impact the performance of ring resonator-based optical filters, particularly in terms of output signal intensity and spectral resolution. These losses are generally divided into two main categories: coupling losses and propagation losses. Coupling losses occur during light transfer from the optical fiber to the silicon waveguides via grating couplers, often due to refractive index mismatch or misalignment. Propagation losses arise as light travels through the waveguides and ring structures and are mainly caused by sidewall roughness, material absorption, and scattering. Both

types of losses reduce the Q-factor, broaden the resonance bandwidth, and degrade wavelength selectivity. Furthermore, the coupling efficiency—which determines how effectively light enters the resonator—is highly sensitive to these losses. Minimizing them through precise optical design and fabrication is essential for achieving high-performance filtering and accurate wavelength discrimination. The amplitude transmission within the ring per round trip is denoted by a, and the round-trip phase shift is $\phi = \beta L$, where L is the circumference of the ring resonator, and β is the propagation constant. The transmission at the through port is given by:

$$T_{\text{Through}} = \frac{a^2 r_2^2 + r_1^2 - 2ar_1 r_2 \cos \phi}{1 + a^2 r_1^2 r_2^2 - 2ar_1 r_2 \cos \phi} \tag{7}$$

The *Drop* port transmission, describing the power transferred from the input waveguide to the side-coupled drop waveguide via the resonator, is expressed as:

$$T_{\text{Drop}} = \frac{a\kappa_1^2 \kappa_2^2}{1 + a^2 r_1^2 r_2^2 - 2ar_1 r_2 \cos \phi}$$
 (8)

Only light whose wavelength matches the resonator's resonance condition is strongly coupled into the ring and transferred to the *Drop* port. This expression reaches a maximum at resonance, where constructive interference facilitates efficient power coupling into the *Drop* port. These equations provide insight into how resonance, losses, and coupling coefficients govern the distribution of optical power in the device.

D. Measurement and Characterization

To assess the performance of the silicon-based ring resonator optical filter, a continuous-wave tunable laser source (CW-TLS) was used as the input, while an optical spectrum analyzer (OSA) was employed to characterize the output response with high precision. The laser source, Keysight 81608A, provides a wavelength tuning range from 1495 nm to 1640 nm and an output power adjustable from 0 to +13 dBm, with a fine control resolution of 0.1 dB. This tool enables accurate wavelength sweeping, particularly across the optical communication bands between 1500 nm and 1600 nm. The laser output was coupled into a single-mode optical fiber (SMF-28 Ultra, Corning), then focused onto the input grating coupler of the photonic chip using a GRIN lens. The angle of incidence was carefully adjusted to 12° relative to the surface normal to optimize coupling efficiency. The fiber used in this experiment, SMF-28e+ (Corning), is designed for low-loss transmission across the 1260-1625 nm wavelength range and is widely used in both C-band (1530-1565 nm) and L-band (1565–1625 nm) applications. With a core diameter of 8.2 µm and a cladding diameter of 125 µm, it provides excellent compatibility with integrated photonic components such as grating couplers and waveguides. The fiber's low attenuation, measured at less than 0.18 dB/km at 1550 nm, ensures minimal signal degradation. After entering the main silicon waveguide (Bus#1), the optical signal interacts sequentially with three ring resonators of identical radius, each positioned laterally at a 0.1 µm gap from Bus#1. These rings are engineered to support resonance at specific wavelengths, allowing a portion

of the optical field to couple into the rings and circulate within them. Under resonant conditions, the light is effectively trapped in the ring structure, leading to enhanced spectral selectivity and narrowband filtering. The resonant signal then couples into the second waveguide (Bus#2) and is directed toward the output grating coupler, where it exits through the *Drop* port. Due to the reciprocal nature of the grating coupler, the output beam emerges at the same 12° angle as the input. A second single-mode fiber, aligned at the same 12° angle, captures the output signal and routes it to the optical spectrum analyzer for spectral analysis. Measurements were conducted using the Yokogawa AQ6370D optical spectrum analyzer, which offers a spectral resolution of 0.02 nm, a dynamic range of 70 dB, and a measurement range from 600 to 1700 nm. The output spectrum from the *Drop* port was recorded over the 1500-1600 nm range. Throughout the experiment, fiber alignment was carefully maintained to ensure measurement consistency and repeatability. To study the effect of ring size on filter performance, three PIC designs were fabricated, each incorporating microring resonators with different radii: 2.5 µm, 3.0 µm, and 3.5 µm. The measured spectral responses, shown in Fig. 2, indicate that increasing the ring radius results in a noticeable shift in the resonance wavelength and changes in the peak intensity. These findings highlight the significant impact of geometric parameters on the filter's spectral behavior and emphasize the importance of precise design for achieving optimal filtering performance. Table I summarizes the key optical characteristics measured at the *Drop* port of the proposed silicon photonic filter. These values were derived from the transmission spectra shown in Fig. 2, providing a comprehensive overview of the filter's spectral performance. Considering the input laser source operates within the wavelength range of 1500-1600 nm, all measurements and analyses were conducted within this spectral region. For the resonators with a radius of 2.5 µm, only two resonance peaks appear at wavelengths of 1532 nm and 1568 nm, with the main resonance wavelength identified at 1568 nm. The limited number of resonant peaks in this case is due to the relatively large FSR of 37 nm, reducing the number of resonances within the measurement window. With a resonance bandwidth $\Delta\lambda$ of 1.99 nm, the measured Qfactor for this radius is 787, and the maximum transmission (T_{Max}) reaches 0.4. Increasing the radius to 3.0 µm leads to four observable resonance peaks at wavelengths of 1505 nm, 1536 nm, 1568 nm, and 1598.7 nm. The maximum resonance peak occurs at wavelength of 1598.7 nm. Due to a reduction of the FSR to 31 nm, more resonance peaks become visible in the measurement range. In this case, the Q-factor increases slightly to 804 while the resonance bandwidth remains constant at 1.99 nm, and the maximum transmission improves to 0.5. For the largest resonator radius of 3.5 µm, four resonance peaks at wavelengths of 1514 nm, 1539 nm, 1567 nm, and 1593 nm are observed, with the main resonance at 1567 nm. Here, the FSR further reduces to 27 nm, resulting in decreased spectral spacing between resonance peaks. The maximum transmission improves to 0.56, while the resonance bandwidth and Q-factor remain nearly identical to the previous cases. Table I clearly indicates that increasing the microring resonator

TABLE I

OPTICAL CHARACTERISTICS AT THE *Drop* PORT OF THE SILICON PHOTONIC FILTER WITH CASCADED MICRORING RESONATORS (RADII: $2.5 \,\mu\text{m}$), as obtained from transmission spectra shown in Fig. 2.

Radius	λ_{p1}	λ_{p2}	λ_{p3}	λ_{p4}	$\lambda_{ m res}$	$\Delta \lambda$	Q-Factor	FSR	T _{Max}
$r=2.5\mu\mathrm{m}$	_	1532	1568	-	1568	1.99	787	37	0.4
$r = 3.0 \mu \text{m}$	1505	1536	1568	1598.7	1598.7	1.99	804	31	0.5
$r=3.5\mu\mathrm{m}$	1514	1539	1567	1593	1567	1.99	787	27	0.56

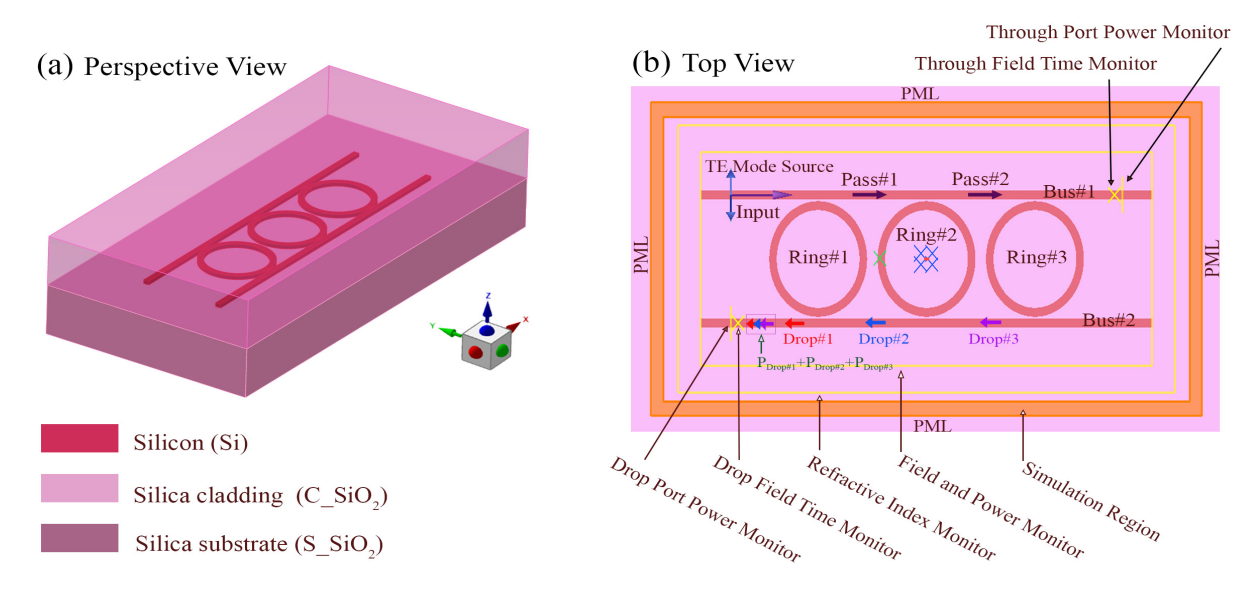


Fig. 3. (a) Perspective view and (b) top view of the simulation setup for the proposed silicon-based ring resonator structure. The device consists of three microring resonators coupled to two parallel straight silicon waveguides encapsulated between a silica cladding and a silica substrate.

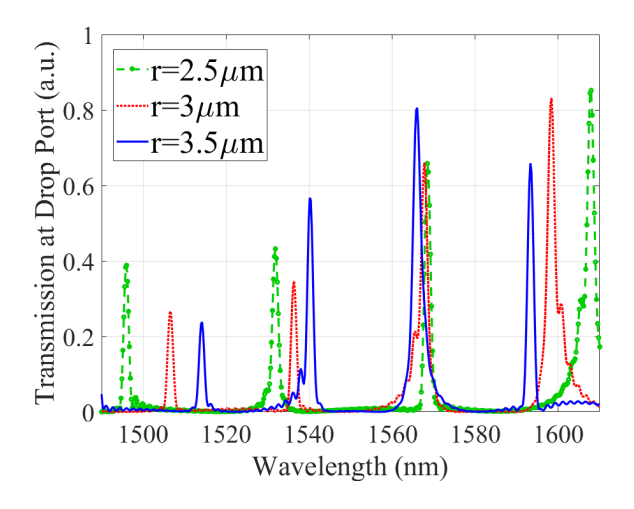


Fig. 4. Transmission spectra at the *Drop* port for ring resonators with radii of 2.5 μ m, 3 μ m, and 3.5 μ m.

radius reduces the FSR, leading to narrower spacing between resonances and an increased number of observable resonance peaks within the wavelength range of 1500–1600 nm.

III. NUMERICAL ANALYSIS

Figure 3(a) presents a perspective view of the simulated design, highlighting the main components, including the straight waveguides and three microring resonators. Figure 3(b) provides the top view, showing the location of the input source

of the TE mode, various monitors (power, field, and refractive index) and the boundaries of the simulation region. In this simulation, only the central part of the filter was modeled, which comprises the ring resonators and the two straight bus waveguides. The grating couplers were omitted to reduce computational complexity and to focus solely on the resonant behavior of the device. These couplers have already been thoroughly studied and characterized in previous literature [50]-[52]. All components of the structure are made of silicon (Si) and are placed on a silica (SiO₂) substrate. A silica upper cladding layer is also included to better replicate the fabricated device and to account for both the effective refractive index profile and the physical protection it provides. The optical properties of the materials used-namely the refractive index (n) and the extinction coefficient (k)—for silicon (Si) and silica (SiO₂) were implemented as wavelength-dependent across the desired operational range, typically within the telecommunication band. These values were extracted from experimental datasets and incorporated into the simulation in the form of spectral material files, enabling a more realistic representation of the waveguide's behavior under actual working conditions. The extinction coefficient (k) quantifies the absorption of optical energy by the material and directly contributes to propagation loss. Although the absorption of silicon in the telecommunication wavelength range is relatively low, it is not negligible, and accounting for it in the simulation is essential for accurately estimating losses. In contrast, silica is considered virtually lossless in this spectral region.

As shown in Fig. 3(b), a mode source is positioned at the input of the upper waveguide (Bus#1) to excite the fundamental TE mode over the wavelength range of 1490 to 1610 nm. The source operates in continuous-wave mode, allowing accurate spectral analysis of the filter's behavior within the optical communication bands. To eliminate unwanted reflections from the simulation boundaries, perfectly matched layer (PML) boundary conditions are applied in all three spatial directions (x, y, and z). This ensures complete absorption of outgoing waves and significantly improves the reliability of the simulation results. The spatial discretization of the simulation domain uses an adaptive non-uniform meshing strategy. Fine mesh cells of 10 nm are applied in critical regions, such as the coupling gaps between the ring resonators and waveguides, where the optical field varies rapidly. Coarser mesh cells of 50 nm are used in less sensitive areas, reducing simulation time without compromising accuracy.

Several monitors are employed throughout the simulation domain to extract meaningful data. Two frequency-domain power monitors are placed at the *Through* and *Drop* ports to capture the transmission spectra at both outputs. Two time-domain monitors are included at the *Through* and *Drop* output ports to observe the temporal behavior of light propagation through the structure. Additionally, one frequency-domain field and power monitor is used to record the distribution of electric and magnetic fields within the coupling regions and inside the rings. This enables a detailed understanding of energy confinement, coupling dynamics, and resonant behavior. A refractive index monitor is also included to observe the wavelength-dependent refractive index values of materials within the structure, providing additional accuracy for modal and spectral analysis.

Due to the sufficiently large center-to-center spacing between adjacent microring resonators in the proposed structure, inter-ring coupling effects are negligible. This spatial separation ensures that each ring operates independently. Consequently, the total optical power at the *Drop* port can be approximated as the sum of the individual power contributions from Drop Ports 1, 2, and 3, as illustrated in Fig. 3(b), and is expressed as:

$$P_{\mathsf{Drop}_T} = P_{\mathsf{Drop}_1} + P_{\mathsf{Drop}_2} + P_{\mathsf{Drop}_3} \tag{9}$$

where

$$\begin{cases} P_{\text{Drop}_1} = T_{\text{Drop}} \cdot P_{\text{input}} \\ P_{\text{Drop}_2} = T_{\text{Drop}} \cdot P_{\text{pass}_1} \\ P_{\text{Drop}_3} = T_{\text{Drop}} \cdot P_{\text{pass}_2} \end{cases}$$
(10)

and the intermediate powers at the pass ports are given by:

$$\begin{cases} P_{\text{pass}_1} = T_{\text{Through}} \cdot P_{\text{input}} \\ P_{\text{pass}_2} = T_{\text{Through}} \cdot P_{\text{pass}_1} \end{cases}$$
 (11)

Substituting these into the expression for total drop power yields:

$$P_{\text{Drop}_T} = T_{\text{Drop}} \cdot \left(1 + T_{\text{Through}} + T_{\text{Through}}^2\right) \cdot P_{\text{input}}$$
 (12)

Therefore, the overall drop-port transmission coefficient is given by:

$$T_{\text{Drop}_T} = \frac{P_{\text{Drop}_T}}{P_{\text{input}}} = T_{\text{Drop}} \left(1 + T_{\text{Through}} + T_{\text{Through}}^2 \right)$$
 (13)

The validity of the analytical model is reinforced by the strong agreement observed between the FDTD simulation results and the experimental measurements of the fabricated device, confirming the assumption that inter-ring coupling is negligible under the given structural configuration.

Figure 4 presents the simulation results for the transmission spectra at the Drop port of the proposed filter structure, evaluated for three configurations with microring resonator radii of $2.5\,\mu m$, $3.0\,\mu m$, and $3.5\,\mu m$. The results clearly show that at specific resonant wavelengths, the input light is efficiently coupled from the upper waveguide into the microring resonators and subsequently transferred to the lower waveguide. This selective routing of light at resonance wavelengths confirms the expected add-drop filtering functionality, validating the effectiveness of the design through numerical simulation.

When compared with the experimental results shown in Fig. 2, the resonance wavelengths observed in the simulation and measurements are nearly identical, indicating strong agreement between the model and the actual fabricated device. However, the resonance peaks in the measured spectra appear lower. This discrepancy is attributed to the presence of two grating couplers in the fabricated structure—one at the input and another at the output-which introduce coupling losses and reduce the overall transmission. Therefore, the simulation in Fig. 4 excludes the grating couplers, resulting in higher transmission peaks due to direct coupling into and out of the waveguides, able II summarizes the optical characteristics at the *Drop* port of the three cascaded microring resonators, corresponding to the simulation results shown in Fig. 4. The analysis is carried out for three different microring radii: 2.5 µm, 3.0 µm, and 3.5 µm. Key parameters such as four resonance wavelengths $(\lambda_{p1}-\lambda_{p4})$, maximum resonance wavelength (λ_{res}), resonance bandwidth ($\Delta\lambda$), Q-factor, FSR, and maximum transmission (T_{Max}) are listed for each configuration. For the smallest radius of 2.5 µm, four resonance peaks are observed at 1496 nm, 1532 nm, 1568 nm, and 1608 nm, with the maximum resonance occurring at 1608 nm. A resonance bandwidth ($\Delta\lambda$) of 2 nm results in a quality factor of 804, while the FSR is measured to be 37.3 nm. The structure exhibits high efficiency, achieving a maximum transmission (T_{Max}) of 0.85. When the radius increases to 3.0 µm, the resonance peaks shift slightly to 1506 nm, 1536 nm, 1568 nm, and 1598 nm, with $\lambda_{\rm res}$ at 1598 nm. The resonance bandwidth remains at 2 nm, while the Q-factor slightly decreases to 799. The FSR narrows to 30.67 nm, and T_{Max} is recorded at 0.83. For the largest radius of 3.5 µm, the resonance peaks appear at 1514 nm, 1540 nm, 1566 nm, and 1593 nm, with λ_{res} centered at 1566 nm and a bandwidth of 2 nm. The Q-factor further decreases to 783, and the FSR reduces to 26.7 nm. A T_{Max} of 0.8 is achieved in this configuration. Table II demonstrates that increasing the microring radius leads to a reduction in the FSR, resulting in a denser distribution of resonance peaks within the target wavelength range. This trend is consistent with

TABLE II

OPTICAL CHARACTERISTICS AT THE *Drop* PORT OF THE SILICON PHOTONIC FILTER WITH CASCADED MICRORING RESONATORS (RADII: $2.5 \,\mu\text{m}$, $3 \,\mu\text{m}$, and $3.5 \,\mu\text{m}$), as obtained from the transmission spectra shown in Fig. 4.

	Radius	λ_{p1} (nm)	λ_{p2} (nm)	λ_{p3} (nm)	$\lambda_{p4} \; (\text{nm})$	$\lambda_{\rm res}$ (nm)	$\Delta\lambda$ (nm)	Q-Factor	FSR (nm)	T_{Max}
ſ	$r=2.5\mu\mathrm{m}$	1496	1532	1568	1608	1608	2	804	37.3	0.85
İ	$r=3.0\mu\mathrm{m}$	1506	1536	1568	1598	1598	2	799	30.67	0.83
Ì	$r = 3.5 \mu\mathrm{m}$	1514	1540	1566	1593	1566	2	783	26.7	0.80

the behavior presented in Table I, indicating that larger radii enable more resonance modes to fall within the operational bandwidth. Although the Q-factor exhibits a slight decrease with increasing radius, the filter consistently maintains high transmission efficiency across all configurations. These simulation results further confirm the expected add-drop filtering behavior and validate the optical performance of the proposed structure, as illustrated in Fig. 4. To further investigate the electromagnetic behavior of the proposed cascaded microring resonator filter, FDTD-based simulations were performed to visualize the spatial distributions of the electric and magnetic fields. Figure 5 presents the steady-state electric field magnitude (|E|, in V/m) in the top three rows (a1–c4) and the corresponding magnetic field magnitude (|H|, in A/m) in the bottom three rows (d1-f4), for ring radii of 2.5 µm, 3.0 µm, and 3.5 µm, each excited at their respective resonant wavelengths. For the 2.5 µm radius, subfigures (a1–a4) and (d1-d4) illustrate the electric and magnetic field distributions at wavelengths of 1496 nm, 1532 nm, 1568 nm, and 1608 nm, respectively. Among these, strong field confinement within and around the microring resonators is particularly evident at 1608 nm, indicating efficient coupling of light from the input waveguide into the rings and subsequently to the *Drop* port. When the radius is increased to 3.0 µm, subfigures (b1b4) and (e1-e4) show the corresponding field distributions at 1507 nm, 1536 nm, 1567 nm, and 1598 nm. As in the previous case, pronounced field localization is observed—especially at 1598 nm—highlighting strong resonance and confirming the structure's ability to perform add-drop filtering across multiple wavelengths. For the 3.5 µm radius, subfigures (c1c4) and (f1-f4) present the field profiles at 1514 nm, 1540 nm, 1566 nm, and 1593 nm. The most prominent field enhancement occurs at 1566 nm, where strong confinement around the microring is again observed. However, a slight reduction in peak field intensity compared to smaller radii is noticeable, which aligns with the modestly decreased transmission efficiency reported in Table II for this configuration. The color bars on the right of each row represent the normalized intensity of the fields, with maximum value shown in red and minimum value in blue. To further evaluate the optical performance of the proposed cascaded microring resonator filter, the power flux (in W/m²) distribution was analyzed for different ring radii and excitation wavelengths. Figure 6 presents the simulated power flux distributions within the structure for radii of 2.5 µm (a1-a4), 3.0 µm (b1-b4), and 3.5 µm (c1-c4). Each subfigure corresponds to a specific resonant wavelength, consistent with the previous spectral and field analysis results. For the 2.5 µm radius, subfigures (a1-a4) show the power flux at wavelengths 1496 nm, 1532 nm, 1568 nm, and 1608 nm, respectively.

Among these, the most significant power transfer through the Drop port is observed at 1608 nm, where the input light is strongly confined and directed through the first ring, confirming effective resonance-based filtering behavior. When the ring radius is increased to 3.0 µm, as shown in subfigures (b1-b4), the strongest power flux appears at 1598 nm. Similar to the previous case, the power is efficiently coupled into the ring resonators and guided toward the *Drop* port, demonstrating the wavelength-selective nature of the filter. For the 3.5 µm radius, the power flux distributions at wavelengths 1514 nm, 1540 nm, 1566 nm, and 1593 nm are depicted in subfigures (c1-c4). The highest power concentration is observed at 1566 nm, with evident coupling into the resonator and extraction through the Drop port. Compared to smaller radii, the spatial spread of the power appears slightly broader, which correlates with the slight decrease in transmission efficiency reported in Table II. The color bar on the right side of each row indicates the normalized power flux intensity, where red represents maximum power flow, and blue indicates minimum. Overall, the power flux distributions in Fig. 6 clearly support the results of the electric and magnetic field simulations (Fig. 5) and the spectral analyses (Figs 2 and 4), confirming the efficient and tunable filtering capability of the proposed photonic structure across different microring radii and wavelengths. Our simulation results verify the wavelength-selective behavior of the proposed ring resonator filter and offer a comprehensive insight into coupling efficiency, field distribution, and spectral performance. These results support the filter's suitability for a wide range of integrated photonic applications, including DWDM, high-resolution optical sensing, and PICs. One of the primary goals in the design of optical filters is to achieve high transmission at specific target wavelengths at the *Drop* port. For optimal performance, these transmission peaks should also exhibit narrow bandwidths, resulting in high Q-factors, which are critical for applications requiring high spectral resolution. In microring resonator design-particularly for racetrack-shaped resonators—the coupling length (L_c) refers to the physical length over which the ring waveguide and the adjacent bus waveguide run parallel to each other at a close separation. This region enables evanescent coupling of optical power between the two waveguides. Unlike circular ring resonators, where coupling occurs at a single point with effectively zero interaction length, racetrack resonators introduce a straight segment to increase the interaction area. By tuning the coupling length, designers can more precisely control the *coupling strength* between the ring and the bus waveguide.

Figure 7(a) shows the transmission spectra as a function of wavelength for ring resonators with different radii. In this

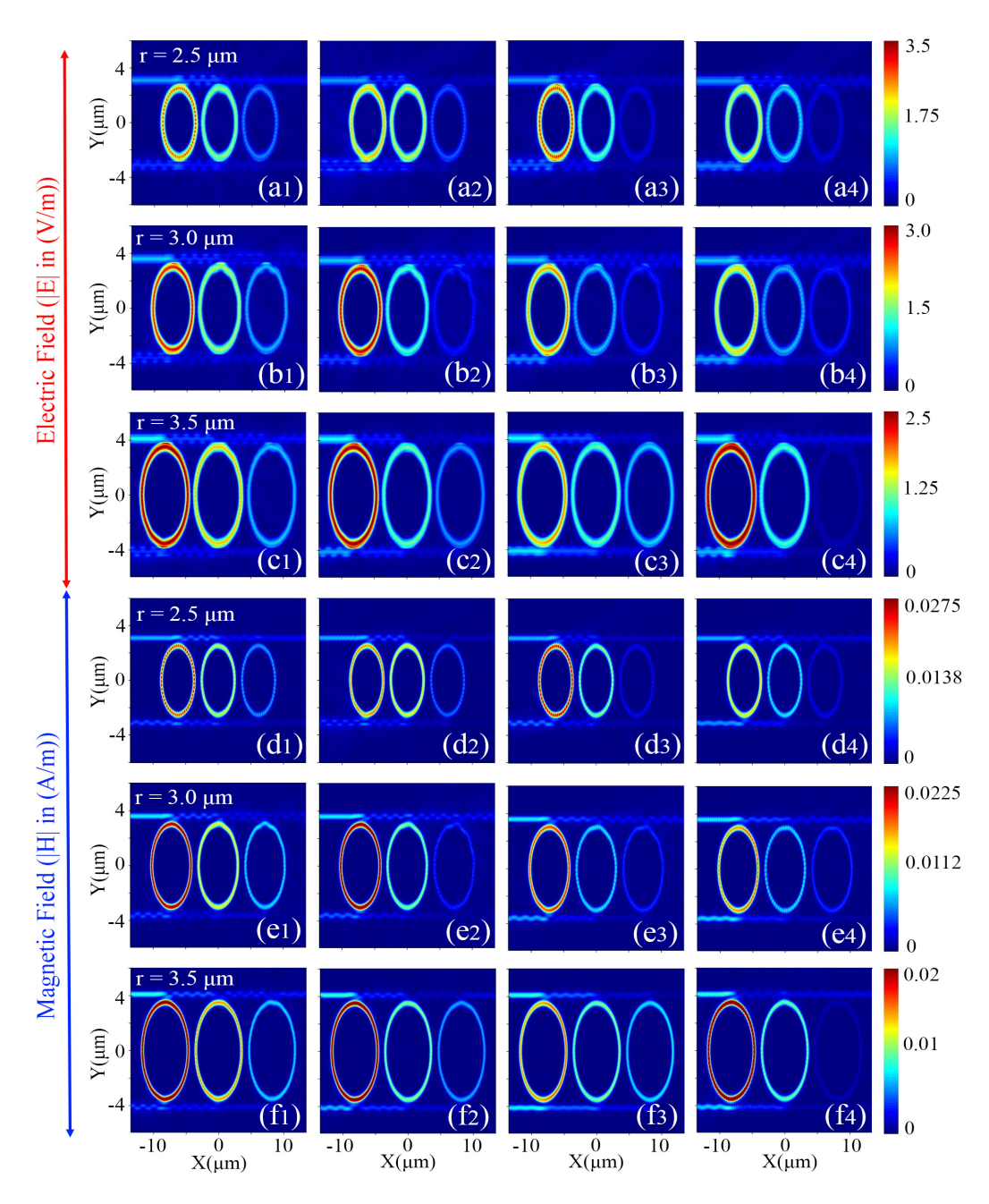


Fig. 5. Electric field (|E|, in V/m) and magnetic field (|H|, in A/m) distributions in cascaded ring resonators for various ring radii and excitation wavelengths. The first three rows (a1–c4) display the electric field intensity distributions, while the last three rows (d1–f4) present the corresponding magnetic field intensity distributions. For radius $r=2.5\,\mu\text{m}$, the subfigures (a1–a4, d1–d4) correspond to wavelengths $\lambda=1496\,\text{nm}$, $1532\,\text{nm}$, $1568\,\text{nm}$, and $1608\,\text{nm}$, respectively. For $r=3.0\,\mu\text{m}$, the subfigures (b1–b4, e1–e4) correspond to $\lambda=1507\,\text{nm}$, $1567\,\text{nm}$, and $1598\,\text{nm}$. For $r=3.5\,\mu\text{m}$, the subfigures (c1–c4, f1–f4) correspond to $\lambda=1514\,\text{nm}$, $1540\,\text{nm}$, $1566\,\text{nm}$, and $1593\,\text{nm}$, respectively. The color bars to the right of each row represent the normalized field intensity, with red indicating the maximum intensity and blue indicating the minimum intensity.

analysis, the waveguide width (denoted as w, representing both the bus and ring waveguide widths), the coupling gap, and the coupling length (L_c) are fixed at 500 nm, 100 nm, and 0 nm, respectively. Numerical simulations based on the FDTD method reveal that increasing the ring radius results in two major effects: (1) a decrease in the amplitude of the transmission peaks, and (2) a reduction in the FSR. These effects can be explained as follows: increasing the radius enlarges the optical path length within the ring, which leads to a higher attenuation and a lower FSR due to the increased

round-trip time. Additionally, a larger radius can reduce the spatial overlap between the optical modes in the bus waveguide and the ring, thereby weakening the coupling efficiency and reducing the peak transmission.

Figure 7(b) illustrates the effect of varying the waveguide width while keeping the ring radius (3.5 μm), coupling gap (100 nm), and coupling length (0 nm) constant. As the waveguide width increases from 490 nm to 520 nm, the resonance peaks shift to longer wavelengths (red-shift), and the transmission amplitude decreases. This shift occurs due to

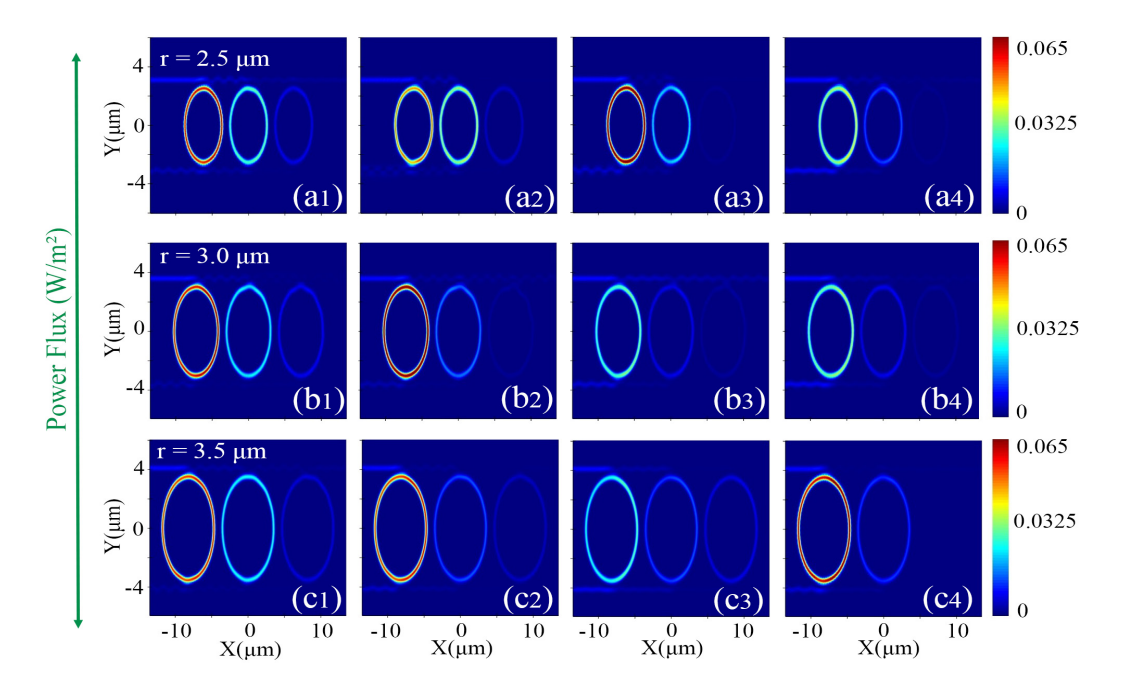


Fig. 6. Power flux (in W/m²) distributions in cascaded ring resonators for different ring radii and operating wavelengths. The three rows correspond to varying ring radii: $r=2.5~\mu m$ (a1-a4), $r=3.0~\mu m$ (b1-b4), and $r=3.5~\mu m$ (c1-c4). Each column represents a different excitation wavelength. Specifically, subfigures (a1-a4) correspond to $\lambda=1496~\rm nm$, $1532~\rm nm$, $1568~\rm nm$, and $1608~\rm nm$; (b1-b4) to $\lambda=1507~\rm nm$, $1536~\rm nm$, $1567~\rm nm$, and $1598~\rm nm$; and (c1-c4) to $\lambda=1514~\rm nm$, $1540~\rm nm$, $1566~\rm nm$, and $1593~\rm nm$, respectively. The color bar on the right side indicates the normalized power flux intensity, where red denotes the highest flux and blue the lowest.

an increase in the effective refractive index of the waveguide, which extends the optical path length. However, the FSR remains nearly unchanged, indicating that the dominant factor influencing the FSR in this configuration is still the ring radius.

Figure 7(c) explores the impact of changing the coupling gap—the physical separation between the bus waveguide and the ring resonator-while maintaining fixed values for the ring radius (3.5 µm), waveguide width (500 nm), and coupling length (0 nm). As the gap decreases from 125 nm to 50 nm, the optical coupling becomes stronger, resulting in increased transmission peak amplitudes and broader resonance bandwidths. This broadening occurs because stronger coupling allows a wider range of wavelengths to couple into the resonator. For applications requiring narrowband filtering, such broadening is undesirable. Conversely, increasing the gap reduces the coupling strength, narrows the bandwidth, and lowers the amplitude of the transmission peaks. Throughout this variation, the FSR remains relatively constant. To further explore the influence of the coupling region on the spectral response of microring filters, we present an analytical study of how the coupling length affects the transmission characteristics. Although our fabricated device and all simulations discussed thus far (Figs 1, 3, 5, and 6) are based on circular microring resonators with zero straight coupling length $L_c = 0$, Fig. 7(d) analyzes the effect of varying the coupling length from 300 nm to 500 nm while keeping the ring radius (3.5 µm), waveguide width (500 nm), and coupling gap (100 nm) constant. As the coupling length increases, more optical power is transferred from the bus waveguide into the ring, leading to higher peak amplitudes and broader bandwidths-similar to the effect of reducing the gap. This broader response negatively impacts the

filter's spectral selectivity. The FSR, however, is not significantly affected by changes in coupling length, as it primarily depends on the round-trip length determined by the ring's radius. These variations in transmission behavior are mainly attributed to changes in the effective refractive index and, consequently, the group index of the structure, both of which are influenced by the geometrical parameters. Based on the above analysis, designers can fine-tune key parameters—including ring radius, waveguide width, coupling gap, and coupling length—to meet desired specifications for resonance wavelength, transmission amplitude, FSR, bandwidth, and Q-factor. Moreover, reducing the number of ring resonators from three to one leads to an approximate 30% decrease in resonance peak amplitude due to the reduced cumulative coupling effect. In multi-ring configurations, maintaining sufficient center-tocenter spacing between adjacent rings is crucial. In this study, a spacing of 8.2 µm was used. If this spacing is reduced below 7.8 µm, undesired inter-ring coupling significantly degrades the transmission peaks, increases bandwidth, and reduces the Q-factor. Table III provides a comparative overview of recently reported microring resonator filters on SOI and other related platforms. Key performance metrics such as Q-factor, FSR, and drop-port efficiency are highlighted. While some structures demonstrate high Q-factors—for example, 20,000 in CMOS-compatible single-ring sensors—they often suffer from limited FSR or reduced drop-port efficiency. On the other hand, PCRRs show exceptionally high simulated efficiencies (up to 99%), but these designs are rarely fabricated, depend on non-standard materials, and are incompatible with typical SOIbased CMOS processes. Additionally, many of the reported works are based solely on simulation, and their performance

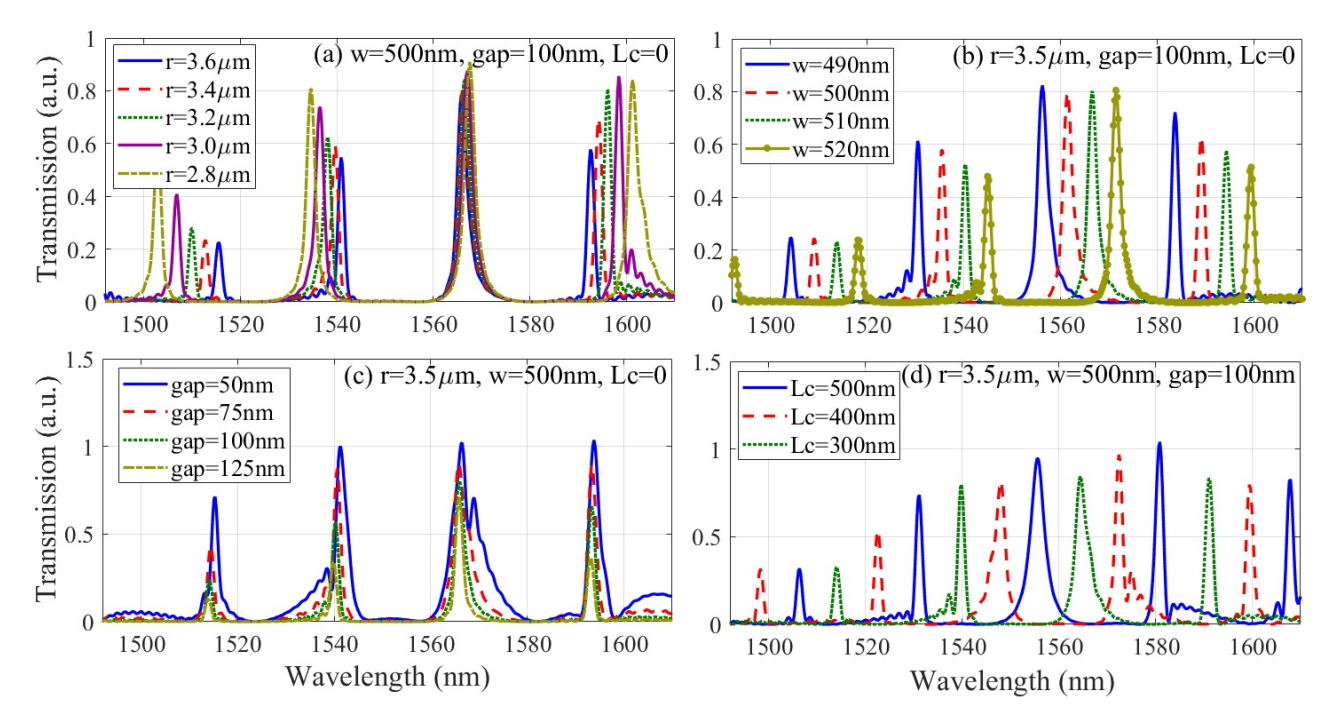


Fig. 7. Transmission spectra at the Drop port of ring resonators under variations in key geometrical parameters: (a) Effect of ring radius variation ($r=2.8-3.6~\mu m$) with fixed waveguide width w=500~nm, gap = 100~nm, and coupling length $L_c=0~nm$. Increasing the radius reduces the free spectral range (FSR) and peak amplitude. (b) Effect of waveguide width variation (w=490-520~nm) with fixed ring radius $r=3.5~\mu m$, gap = 100~nm, and $L_c=0~nm$. Increasing the waveguide width causes a red-shift in resonance peaks and reduces the peak amplitude. (c) Effect of coupling gap variation (gap = 50-125~nm) with fixed $r=3.5~\mu m$, w=500~nm, and $L_c=0~nm$. Smaller gaps enhance coupling, leading to broader resonance bandwidth and higher peak transmission. (d) Effect of coupling length variation ($L_c=300-500~nm$) with fixed $r=3.5~\mu m$, w=500~nm, and gap = 100~nm. Increasing L_c increases the coupling strength, resulting in wider resonance peaks and higher amplitudes.

remains unverified until physical fabrication and experimental validation are performed. In contrast, our proposed cascaded microring filter has been both simulated and fabricated on a standard SOI platform, achieving a well-balanced performance in terms of a relatively large FSR (27-37 nm) and high dropport efficiency. Specifically, the design achieved 85% drop efficiency in simulation and 56% in the fabricated device, where the latter includes the impact of input and output grating couplers. To isolate the intrinsic performance of the filter itself, we removed the influence of the grating couplers from the total measured transmission. Because the input and output grating couplers are identical and their spectral responses are well characterized [53]–[56], we were able to de-embed their effect from the measured results. This analysis revealed a corrected drop-port efficiency of approximately 83% for the fabricated device, closely aligning with the simulated result. This final case, presented in the last row of Table III, represents the true optical performance of our fabricated filter and demonstrates its strong potential for deployment in DWDM systems and PICs.

IV. CONCLUSION

This work presented the comprehensive design, fabrication, and analysis of a cascaded triple microring resonator filter implemented on a silicon-on-insulator platform. Through systematic variation of key structural parameters, including the radius of the ring, the coupling gap, the coupling length, and the waveguide width, the spectral characteristics of the

filter were fine-tuned. The device was fabricated using highresolution electron beam lithography. Experimental characterization across the 1500-1600 nm window demonstrated multiple sharp resonance peaks with high transmission efficiency and excellent alignment with FDTD-based simulations, confirming the reliability of the design and the accuracy of the fabrication process. Notably, the device exhibited high Qfactors, narrow passbands, and low insertion loss, demonstrating strong potential for integration into advanced photonic systems. Field and power flux distributions provided further insight into the resonant behavior and coupling dynamics, revealing efficient mode confinement and selective wavelength routing at resonance. These results lay a strong foundation for the development of compact, high-resolution photonic filters compatible with CMOS technology. Owing to their favorable characteristics, these filters hold great promise for integration into PICs aimed at dense wavelength-division multiplexing, on-chip routing, and high-resolution optical signal processing. The results not only validate the effectiveness of the design methodology, but also demonstrate the potential for advancing toward more sophisticated and tunable filtering architectures. Future research may focus on incorporating active tuning techniques, such as thermal or electro-optic modulation, to enhance functionality and enable dynamic reconfigurability in emerging optical networks and integrated photonic platforms.

REFERENCES

[1] S. Kaur, P. Singh, V. Tripathi, and R. Kaur, "Recent trends in wireless and optical fiber communication," *Global Transitions Proceedings*,

Reference Structure Type		Platform	Method	Q-factor	FSR (nm)	Efficiency	Notes	
[36]	Single MRR	LNOI	Sim. + Fab.	7500	2.5	50%	Non-SOI platform	
[42]	PC Ring Resonator	2D PhC	Simulation	3104	_	99%	Simulated only	
[15]	PC Ring Resonator	2D PhC	Simulation	160-1000	30	82%	High FSR, low Q	
[57]	Single Drop-ring	SOI	Simulation	250	20	65%	Review-based	
[28]	CMOS-compatible MRR	SOI	Fabrication	20000	23.4	35%	Ultra-high Q	
This work (simulated)	Cascaded ring Resonators	SOI	Simulation	804	27–37	85%	Without grating couplers	
This work (fabricated)	Cascaded ring Resonators	SOI	Fabrication	804	27–37	56%	With grating couplers	
This work (fabricated)	Cascaded ring Resonators	SOI	Fabrication	804	27–37	83%	Without grating couplers	

TABLE III

COMPARISON OF RECENTLY REPORTED MICRORING RESONATOR FILTERS WITH OUR PROPOSED WORK

- vol. 3, no. 1, pp. 343-348, 2022.
- [2] J. Yu and J. Zhang, "Recent progress on high-speed optical transmission," *Digital communications and networks*, vol. 2, no. 2, pp. 65–76, 2016
- [3] E. Agrell, M. Karlsson, A. Chraplyvy, D. J. Richardson, P. M. Krummrich, P. Winzer, K. Roberts, J. K. Fischer, S. J. Savory, B. J. Eggleton et al., "Roadmap of optical communications," *Journal of optics*, vol. 18, no. 6, p. 063002, 2016.
- [4] I. Amiri, A. N. Z. Rashed, and P. Yupapin, "High-speed transmission circuits signaling in optical communication systems," *Journal of Optical Communications*, vol. 45, no. s1, pp. s69–s75, 2024.
- [5] M. J. Heck, J. F. Bauters, M. L. Davenport, J. K. Doylend, S. Jain, G. Kurczveil, S. Srinivasan, Y. Tang, and J. E. Bowers, "Hybrid silicon photonic integrated circuit technology," *IEEE Journal of Selected Topics* in *Quantum Electronics*, vol. 19, no. 4, pp. 6100117–6100117, 2012.
- [6] L. A. Coldren, S. W. Corzine, and M. L. Mashanovitch, *Diode lasers and photonic integrated circuits*. John Wiley & Sons, 2012.
- [7] D. Dai, L. Liu, S. Gao, D.-X. Xu, and S. He, "Polarization management for silicon photonic integrated circuits," *Laser & Photonics Reviews*, vol. 7, no. 3, pp. 303–328, 2013.
- [8] F. Kish, V. Lal, P. Evans, S. W. Corzine, M. Ziari, T. Butrie, M. Reffle, H.-S. Tsai, A. Dentai, J. Pleumeekers et al., "System-on-chip photonic integrated circuits," *IEEE Journal of Selected Topics in Quantum Elec*tronics, vol. 24, no. 1, pp. 1–20, 2017.
- [9] S. C. Xavier, B. E. Carolin, A. P. Kabilan, and W. Johnson, "Compact photonic crystal integrated circuit for all-optical logic operation," *IET Optoelectronics*, vol. 10, no. 4, pp. 142–147, 2016.
- [10] P. Dong, "Silicon photonic integrated circuits for wavelength-division multiplexing applications," *IEEE Journal of Selected Topics in Quantum Electronics*, vol. 22, no. 6, pp. 370–378, 2016.
- [11] S. J. McNab, N. Moll, and Y. A. Vlasov, "Ultra-low loss photonic integrated circuit with membrane-type photonic crystal waveguides," *Optics express*, vol. 11, no. 22, pp. 2927–2939, 2003.
- [12] J. Yang, M. Tang, S. Chen, and H. Liu, "From past to future: onchip laser sources for photonic integrated circuits," *Light: Science & Applications*, vol. 12, no. 1, p. 16, 2023.
- [13] G.-H. Duan, C. Jany, A. Le Liepvre, A. Accard, M. Lamponi, D. Make, P. Kaspar, G. Levaufre, N. Girard, F. Lelarge *et al.*, "Hybrid iii–v on silicon lasers for photonic integrated circuits on silicon," *IEEE Journal* of selected topics in quantum electronics, vol. 20, no. 4, pp. 158–170, 2014.
- [14] M. Djavid and M. Abrishamian, "Multi-channel drop filters using photonic crystal ring resonators," *Optik*, vol. 123, no. 2, pp. 167–170, 2012.
- [15] Z. Qiang, W. Zhou, and R. A. Soref, "Optical add-drop filters based on photonic crystal ring resonators," *Optics express*, vol. 15, no. 4, pp. 1823–1831, 2007.
- [16] M. Djavid, A. Ghaffari, F. Monifi, and M. S. Abrishamian, "T-shaped channel-drop filters using photonic crystal ring resonators," *Physica E: Low-dimensional Systems and Nanostructures*, vol. 40, no. 10, pp. 3151–3154, 2008.
- [17] G. Antonacci, K. Elsayad, and D. Polli, "On-chip notch filter on a silicon nitride ring resonator for brillouin spectroscopy," ACS Photonics, vol. 9, no. 3, pp. 772–777, 2022.
- [18] C. Ciminelli, F. Dell'Olio, G. Brunetti, D. Conteduca, and M. N. Armenise, "New microwave photonic filter based on a ring resonator including a photonic crystal structure," in 2017 19th International Conference on Transparent Optical Networks (ICTON). IEEE, 2017, pp. 1–4.
- [19] G. Brunetti, N. Sasanelli, M. N. Armenise, and C. Ciminelli, "High performance and tunable optical pump-rejection filter for quantum

- photonic systems," Optics & Laser Technology, vol. 139, p. 106978, 2021.
- [20] F. Qiu and Y. Han, "Electro-optic polymer ring resonator modulators," Chinese optics letters, vol. 19, no. 4, p. 041301, 2021.
- [21] G. Li, A. V. Krishnamoorthy, I. Shubin, J. Yao, Y. Luo, H. Thacker, X. Zheng, K. Raj, and J. E. Cunningham, "Ring resonator modulators in silicon for interchip photonic links," *IEEE Journal of Selected Topics* in *Quantum Electronics*, vol. 19, no. 6, pp. 95–113, 2013.
- [22] D. G. Rabus, C. Sada, D. G. Rabus, and C. Sada, "Ring resonators: Theory and modeling," *Integrated Ring Resonators: A Compendium*, pp. 3–46, 2020.
- [23] J. K. Poon, J. Scheuer, Y. Xu, and A. Yariv, "Designing coupledresonator optical waveguide delay lines," *Journal of the Optical Society* of America B, vol. 21, no. 9, pp. 1665–1673, 2004.
- [24] M. S. Rasras, C. K. Madsen, M. A. Cappuzzo, E. Chen, L. T. Gomez, E. J. Laskowski, A. Griffin, A. Wong-Foy, A. Gasparyan, A. Kasper et al., "Integrated resonance-enhanced variable optical delay lines," *IEEE* photonics technology letters, vol. 17, no. 4, pp. 834–836, 2005.
- [25] L. Zhuang, M. Hoekman, W. Beeker, A. Leinse, R. Heideman, P. van Dijk, and C. Roeloffzen, "Novel low-loss waveguide delay lines using vernier ring resonators for on-chip multi-λ microwave photonic signal processors," *Laser & photonics reviews*, vol. 7, no. 6, pp. 994–1002, 2013.
- [26] X. Fan, I. M. White, H. Zhu, J. D. Suter, and H. Oveys, "Overview of novel integrated optical ring resonator bio/chemical sensors," in *Laser Resonators and Beam Control IX*, vol. 6452. SPIE, 2007, pp. 166–185.
- [27] R. Rajasekar and S. Robinson, "Nano-pressure and temperature sensor based on hexagonal photonic crystal ring resonator," *Plasmonics*, vol. 14, pp. 3–15, 2019.
- [28] G.-D. Kim, H.-S. Lee, C.-H. Park, S.-S. Lee, B. T. Lim, H. K. Bae, and W.-G. Lee, "Silicon photonic temperature sensor employing a ring resonator manufactured using a standard cmos process," *Optics express*, vol. 18, no. 21, pp. 22215–22221, 2010.
- [29] L. Huang, H. Tian, D. Yang, J. Zhou, Q. Liu, P. Zhang, and Y. Ji, "Optimization of figure of merit in label-free biochemical sensors by designing a ring defect coupled resonator," *Optics Communications*, vol. 332, pp. 42–49, 2014.
- [30] L. Hajshahvaladi, H. Kaatuzian, and M. Danaie, "A very high-resolution refractive index sensor based on hybrid topology of photonic crystal cavity and plasmonic nested split-ring resonator," *Photonics and Nanostructures-Fundamentals and Applications*, vol. 51, p. 101042, 2022
- [31] P. Steglich, D. G. Rabus, C. Sada, M. Paul, M. G. Weller, C. Mai, and A. Mai, "Silicon photonic micro-ring resonators for chemical and biological sensing: A tutorial," *IEEE sensors journal*, vol. 22, no. 11, pp. 10089–10105, 2021.
- [32] J. Haavisto and G. Pajer, "Resonance effects in low-loss ring waveguides," *Optics Letters*, vol. 5, no. 12, pp. 510–512, 1980.
- [33] D. Rafizadeh, J. Zhang, S. Hagness, A. Taflove, K. Stair, S. Ho, and R. Tiberio, "Waveguide-coupled algaas/gaas microcavity ring and disk resonators with high finesse and 21.6-nm free spectral range," *Optics letters*, vol. 22, no. 16, pp. 1244–1246, 1997.
- [34] R. Grover, V. Van, T. Ibrahim, P. Absil, L. Calhoun, F. Johnson, J. Hryniewicz, and P.-T. Ho, "Parallel-cascaded semiconductor microring resonators for high-order and wide-fsr filters," *Journal of Lightwave Technology*, vol. 20, no. 5, p. 872, 2002.
- [35] W. Bogaerts, P. De Heyn, T. Van Vaerenbergh, K. De Vos, S. Kumar Selvaraja, T. Claes, P. Dumon, P. Bienstman, D. Van Thourhout, and R. Baets, "Silicon microring resonators," *Laser & Photonics Reviews*, vol. 6, no. 1, pp. 47–73, 2012.

- [36] I. Krasnokutska, J.-L. J. Tambasco, and A. Peruzzo, "Tunable large free spectral range microring resonators in lithium niobate on insulator," *Scientific reports*, vol. 9, no. 1, p. 11086, 2019.
- [37] M. A. Tran, D. Huang, J. Guo, T. Komljenovic, P. A. Morton, and J. E. Bowers, "Ring-resonator based widely-tunable narrow-linewidth si/inp integrated lasers," *IEEE Journal of Selected Topics in Quantum Electronics*, vol. 26, no. 2, pp. 1–14, 2019.
- [38] M. A. Selim and M. Anwar, "Enhanced q-factor and effective length silicon photonics filter utilizing nested ring resonators," *Journal of Optics*, vol. 25, no. 11, p. 115801, 2023.
- [39] N. Saha, G. Brunetti, A. di Toma, M. N. Armenise, and C. Ciminelli, "Silicon photonic filters: A pathway from basics to applications," *Advanced Photonics Research*, vol. 5, no. 10, p. 2300343, 2024.
- [40] M. Y. Mahmoud, G. Bassou, A. Taalbi, and Z. M. Chekroun, "Optical channel drop filters based on photonic crystal ring resonators," *Optics* communications, vol. 285, no. 3, pp. 368–372, 2012.
- [41] V. D. Kumar, T. Srinivas, and A. Selvarajan, "Investigation of ring resonators in photonic crystal circuits," *Photonics and Nanostructures-Fundamentals and Applications*, vol. 2, no. 3, pp. 199–206, 2004.
- [42] H. Alipour-Banaei and F. Mehdizadeh, "High sensitive photonic crystal ring resonator structure applicable for optical integrated circuits," *Pho*tonic Network Communications, vol. 33, pp. 152–158, 2017.
- [43] Y. Liu, Y. Yu, L. Wang, Y. Yu, and X. Zhang, "Reconfigurable microwave photonic bandpass filter based on crow," *Journal of Lightwave Technology*, vol. 42, no. 5, pp. 1597–1604, 2023.
- [44] S. Romero-García, A. Moscoso-Mártir, J. Müller, B. Shen, F. Merget, and J. Witzens, "Wideband multi-stage crow filters with relaxed fabrication tolerances," *Optics express*, vol. 26, no. 4, pp. 4723–4737, 2018.
- [45] R. R. Kumar and H. K. Tsang, "High-extinction crow filters for scalable quantum photonics," *Optics Letters*, vol. 46, no. 1, pp. 134–137, 2021.
- [46] Z. Cheng, J. Zhang, J. Dong, and Y. Ding, "Compact high-contrast silicon optical filter using all-passive and crow fano nanobeam resonators," Optics Letters, vol. 46, no. 16, pp. 3873–3876, 2021.
- [47] H. Saghaei, P. Elyasi, and R. Karimzadeh, "Design, fabrication, and characterization of mach-zehnder interferometers," *Photonics and Nanostructures-Fundamentals and Applications*, vol. 37, p. 100733, 2019.
- [48] H. Saghaei, P. Elyasi, and B. J. Shastri, "Sinusoidal and rectangular bragg grating filters: Design, fabrication, and comparative analysis," *Journal of Applied Physics*, vol. 132, no. 6, 2022.
- [49] V. Van, Optical microring resonators: theory, techniques, and applications. CRC Press, 2016.
- [50] L. Cheng, S. Mao, Z. Li, Y. Han, and H. Fu, "Grating couplers on silicon photonics: Design principles, emerging trends and practical issues," *Micromachines*, vol. 11, no. 7, p. 666, 2020.
- [51] Y. Tang, Z. Wang, L. Wosinski, U. Westergren, and S. He, "Highly efficient nonuniform grating coupler for silicon-on-insulator nanophotonic circuits," *Optics letters*, vol. 35, no. 8, pp. 1290–1292, 2010.
- [52] D. Taillaert, P. Bienstman, and R. Baets, "Compact efficient broadband grating coupler for silicon-on-insulator waveguides," *Optics letters*, vol. 29, no. 23, pp. 2749–2751, 2004.
- [53] W. Shi, X. Wang, C. Lin, H. Yun, Y. Liu, T. Baehr-Jones, M. Hochberg, N. A. Jaeger, and L. Chrostowski, "Silicon photonic grating-assisted, contra-directional couplers," *Optics express*, vol. 21, no. 3, pp. 3633– 3650, 2013.
- [54] W. Shi, V. Veerasubramanian, D. V. Plant, N. A. Jaeger, and L. Chrostowski, "Silicon photonic bragg-grating couplers for optical communications," in *Next-Generation Optical Networks for Data Centers and Short-Reach Links*, vol. 9010. SPIE, 2014, pp. 63–74.
- [55] Y. Wang, X. Wang, J. Flueckiger, H. Yun, W. Shi, R. Bojko, N. A. Jaeger, and L. Chrostowski, "Focusing sub-wavelength grating couplers with low back reflections for rapid prototyping of silicon photonic circuits," *Optics express*, vol. 22, no. 17, pp. 20652–20662, 2014.
- [56] A. Mekis, S. Gloeckner, G. Masini, A. Narasimha, T. Pinguet, S. Sahni, and P. De Dobbelaere, "A grating-coupler-enabled cmos photonics platform," *IEEE Journal of Selected Topics in Quantum Electronics*, vol. 17, no. 3, pp. 597–608, 2010.
- [57] Y. R. Bawankar and A. Singh, "Microring resonators based applications in silicon photonics-a review," in 2021 5th conference on information and communication technology (CICT). IEEE, 2021, pp. 1–6.



Hamed Saghaei received the B.Sc., M.Sc., and Ph.D. degrees in electrical engineering in 2004, 2007, and 2015, respectively. He is currently a guest researcher in the Department of Electrical and Computer Engineering at the University of Alberta, Edmonton, AB, Canada. His work spans a diverse range of photonic and electromagnetic systems, with a particular focus on silicon photonics, photonic crystal devices, advanced antenna design, and energy-harvesting technologies such as next-generation solar cells. Dr. Saghaei is a Topical Editor

for the *JOSA B* and has authored numerous peer-reviewed publications in optics, photonics, and applied electromagnetics. He is passionate about bridging theoretical insight with practical device implementation to enable compact, high-performance solutions for modern communication, sensing, and energy systems.



Kambiz Moez (Senior Member, IEEE) received the B.Sc. degree in electrical engineering from the University of Tehran, Tehran, Iran, in 1999, and the M.Sc. and Ph.D. degrees from the University of Waterloo, Waterloo, ON, Canada, in 2002 and 2006, respectively. Since January 2007, he has been with the Department of Electrical and Computer Engineering, University of Alberta, Edmonton, AB, Canada, where he is currently a Professor. His research interests include the analysis and design of analog, radio frequency, and millimeter-wave

CMOS integrated circuits and systems for a variety of applications, including wired/wireless communications, biomedical imaging, instrumentation, radar systems, and power electronics. He is currently serving as an Associate Editor for the *IEEE Transactions on Circuits and Systems I: Regular Papers* and *IET Electronics Letters*. He is also a registered Professional Engineer in the Province of Alberta.